Nuclear Instruments and Methods in Physics Research A330 (1993) 389–404
North-Holland

NUCLEAR
INSTRUMENTS
& METHODS
IN PHYSICS
RESEARCH
Section A

Measurement of the time development of particle showers in a uranium scintillator calorimeter

A. Caldwell, L. Hervás [1], J.A. Parsons, F. Sciulli, W. Sippach and L. Wai
Nevis Labs, Columbia University, P.O. Box 137, Irvington, NY 10533, USA

Received 24 November 1992

We report on the time evolution of particle showers, as measured in modules of the uranium–scintillator barrel calorimeter of the ZEUS detector. The time development of hadronic showers differs significantly from that of electromagnetic showers, with about 40% of the response to hadronic showers arising from energy depositions which occur late in the shower development. The degree of compensation and the hadronic energy resolution were measured as a function of integration time, giving a value of $e/\pi = 1.02 \pm 0.01$ for a gate width of 100 ns. The possibilities for electron–hadron separation based on the time structure of the shower were studied, with pion rejection factors in excess of 100 being achieved for electron efficiencies greater than 60%. The custom electronics used to perform these measurements samples the calorimeter signal at close to 60 MHz, stores all samples for a period of over 4 μs using analog switched capacitor pipelines, and digitizes the samples for triggered events with 12-bit ADCs.

1. Introduction

The calorimeter of the ZEUS detector was designed for optimal hadronic energy resolution. Depleted uranium was chosen as the absorber material, with organic scintillator as the sampling medium, in order to achieve equal responses to electromagnetic and hadronic showers. One of the consequences of this choice is the presence in hadronic showers of energy depositions on long time scales. We report in this paper on detailed measurements of the time evolution of showers in ZEUS calorimeter modules. The results shed light on the mechanism of compensation, the influence of the degree of compensation on the hadronic energy resolution, possibilities to perform electron–pion separation based on timing information, and implications of the long time components for pile-up noise in a high rate environment.

This paper is organized as follows: Section 2 reviews the arguments for designing a compensating calorimeter, and describes the expected sources of long time components in a uranium–scintillator sampling calorimeter. A brief description of the structure of the ZEUS calorimeter modules used in this study is presented in section 3. The custom electronics designed and constructed for this test are described in detail in section 4, followed in section 5 by a description of the testbeam setup at FNAL. We then report in section 6 on the measurements performed, including results on the time response for laser pulses, electron showers, and hadron showers. The measured hadron shower time spectra are deconvoluted in order to extract the deposited energy time profile, which is compared to Monte Carlo predictions. The ratio of electron to hadron response is measured as a function of integration time, as is the hadronic energy resolution. Finally, the different time structures of electromagnetic and hadronic showers are used as a tool for electron–pion separation. Section 7 summarizes the conclusions of the study.

2. Background

The role of calorimetry has become increasingly prominent in high energy physics experiments as the energies of the particles to be detected has increased. This results from the fact that the relative resolution obtainable with calorimetric techniques improves with energy, and that the depth of the calorimeter required to contain particle showers increases only logarithmically with the incident particles' energy. The increasing importance of jet physics, and the subsequent need to measure not only charged but also neutral particles, has contributed as well to strengthening the role of calorimetry.

While the physics of electromagnetic calorimetry is well understood, hadronic showers are considerably more complicated. It is known that when a hadron

[1] Univ. Autónoma de Madrid, Spain (supported by CICYT).

interacts in a calorimeter, some of its energy is deposited in an electromagnetic component of the shower, predominantly through the production of π^0 mesons. Additional energy is lost through dE/dx processes. The remaining, purely hadronic, energy loss mechanisms include not only the production of a cascade of charged pions and other particles, but also energy which is lost to nuclear binding energy, nuclear recoil energy, the production of neutrons, and other nuclear processes. Some or all of the energy absorbed in these processes does not contribute to the signal, and is thus "invisible"; as a result, the ratio of the electromagnetic to purely hadronic responses is typically greater than unity ($e/h > 1$).

The value of e/h has important consequences for the behavior of a hadron calorimeter. The fractional contribution of the electromagnetic component of a hadron shower depends strongly on the nature of the

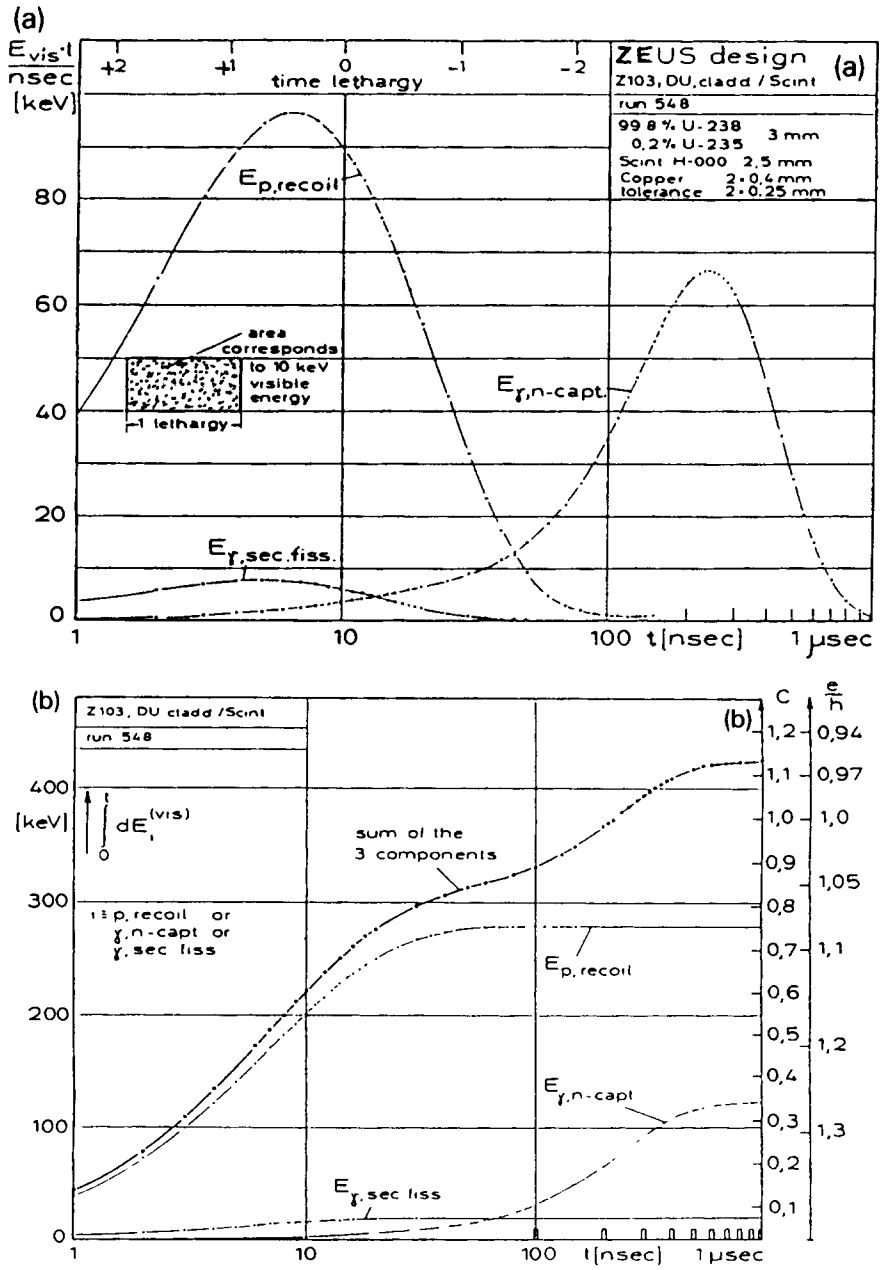

Fig. 1. (a) Lethargy plot showing the predicted time spectrum of the late components of a hadron shower for a calorimeter similar to that of the ZEUS detector. (b) Integrated late response using the predictions of (a). Both plots are from ref. [4].

first few interactions, and therefore exhibits large non-Gaussian fluctuations. For a calorimeter with a value of e/h differing from unity, these fluctuations contribute significantly to, and can easily dominate, the hadronic resolution, resulting in it being substantially worse than the electromagnetic energy resolution. In addition, they produce a deviation of the energy resolution from the $1/\sqrt{E}$ behavior, limiting the resolution at high hadron energies. The fact that the fractional contribution of the electromagnetic component rises with energy also implies that a calorimeter with a value of e/h differing from unity will exhibit a nonlinearity in the hadron response.

These issues led to the proposal [1] to convert some of the invisible hadronic energy to a measurable signal to achieve an equal response to the electromagnetic and hadronic components ($e/h = 1$), a condition known as "compensation". A compensating calorimeter could exhibit a linear hadron response as well as a hadronic energy resolution which scales with $1/\sqrt{E}$. In addition, having removed the contribution from the fluctuations in π^0 production results in a significantly improved hadronic energy resolution.

In recent years, there has been considerable progress in the understanding of hadronic showers. Indeed, extensive test programs [2], combined with detailed Monte Carlo (MC) simulations [3–5], have made possible the design and construction of very large compensating calorimeters, such as that of the ZEUS detector [6]. For the uranium–scintillator ZEUS calorimeter, the response to a hadronic shower is expected to comprise several contributions. These include the electromagnetic component, ionization losses, and several mechanisms which are initiated by the many neutrons with kinetic energy in the few MeV range which are released in the hadronic shower. Measuring the time evolution of the response to hadronic showers provides a sensitive method for deconvoluting the various energy loss mechanisms, as their signals are expected to be collected on very different time scales. The $\mathrm{d}E/\mathrm{d}x$ and electromagnetic shower components should be prompt (≈ 0 ns). Delayed components include signals from "free" protons in the scintillator recoiling after a collision with a neutron, as well as from photons from secondary fission (both ≈ 0–100 ns). In addition, a late contribution (≈ 10–1000 ns) due to photons resulting from de-excitation of heavy nuclei after thermal neutron capture is expected.

Fig. 1a shows a MC prediction [4] of the time spectrum of the delayed hadronic energy depositions for a calorimeter very similar to that of the ZEUS detector. The prediction for 10 GeV pions is shown on a "lethargy plot", where the product of the energy and the time, Et, is plotted versus $\log(t)$. In such a plot, equal areas correspond to equal energy depositions. In fig. 1b, the integrated response is shown as a function of integration time. The figures indicate that the largest component of the hadron response is expected from proton recoil in the scintillator, with photons from secondary fission contributing relatively little. The component due to photons produced in the de-excitation of nuclei following thermal neutron capture is also predicted to be quite large, contributing most significantly at times greater than 100 ns.

While the existence of late energy deposits in hadronic showers has been verified by several groups [7], no precise measurements are available. This paper reports the results of a detailed experimental study of the time development of particle showers in ZEUS barrel calorimeter modules, updating and extending preliminary results which have been previously reported [8].

3. Calorimeter

The measurements described here were performed during the 1991 fixed target running period at FNAL, using 4 ZEUS barrel calorimeter (BCAL) modules [9] stacked together. The complete BCAL, providing full azimuthal coverage, comprises 32 identical wedge-shaped modules; our setup thus corresponds to one octant of the ZEUS BCAL. Each module (see fig. 2) is constructed of interleaved plates of scintillator (SCI) and stainless-steel clad depleted uranium (DU), with the SCI light transmitted via wavelength-shifter (WLS) material to photomultiplier tubes (PMT) for conversion to an electrical signal. The SCI material is SCSN-38 while the WLS is Y-7 doped PMMA. Refs. [6,10] should be consulted for more details on the optical components.

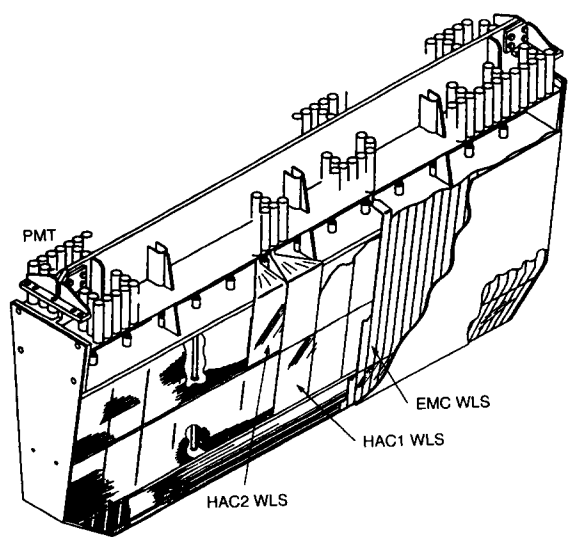

Fig. 2. Isometric view of a single ZEUS BCAL module.

Each BCAL module is segmented into three longitudinal sections. The front section, forming the electromagnetic calorimeter (EMC), is approximately one interaction length (1λ) in depth, corresponding to about 22 radiation lengths. It is followed by the two separate hadronic sections (HAC1 and HAC2), each of which contains an additional 2λ. A BCAL module is divided transversely into 14 towers. A single tower, measuring approximately 20 cm $\times$ 20 cm at the front face, contains four EMC cells, one HAC1 cell, and one HAC2 cell. Each cell of the calorimeter is read out by two PMTs, one on each side of the stack.

For this measurement, 192 channels of custom electronics were built, sufficient to instrument almost six full towers of each of the four BCAL modules. The transverse dimensions of the instrumented region were approximately 1 m $\times$ 1 m at the front face, increasing to about 1.8 m $\times$ 1.4 m at the back, with a depth slightly in excess of five interaction lengths. The transverse size was more than adequate to contain the showers, while longitudinal leakage was monitored by reading out a tail-catcher behind the BCAL modules.

4. Electronic readout

In order to study in detail the time development of hadronic showers, both on average and event-by-event, we designed and constructed electronics [11] which: 1) performs a dc integration of the PMT signal; 2) samples the integrated signal every 18 ns; 3) stores the samples in a 4 μs long analog pipeline; and 4) digitizes the samples for triggered events with 12-bit ADCs. Table 1 summarizes some of the properties of the electronics.

A schematic of a single channel of the analog electronics is shown in fig. 3a. The signal from the PMT is dc-coupled to an integrator. The integrator output is

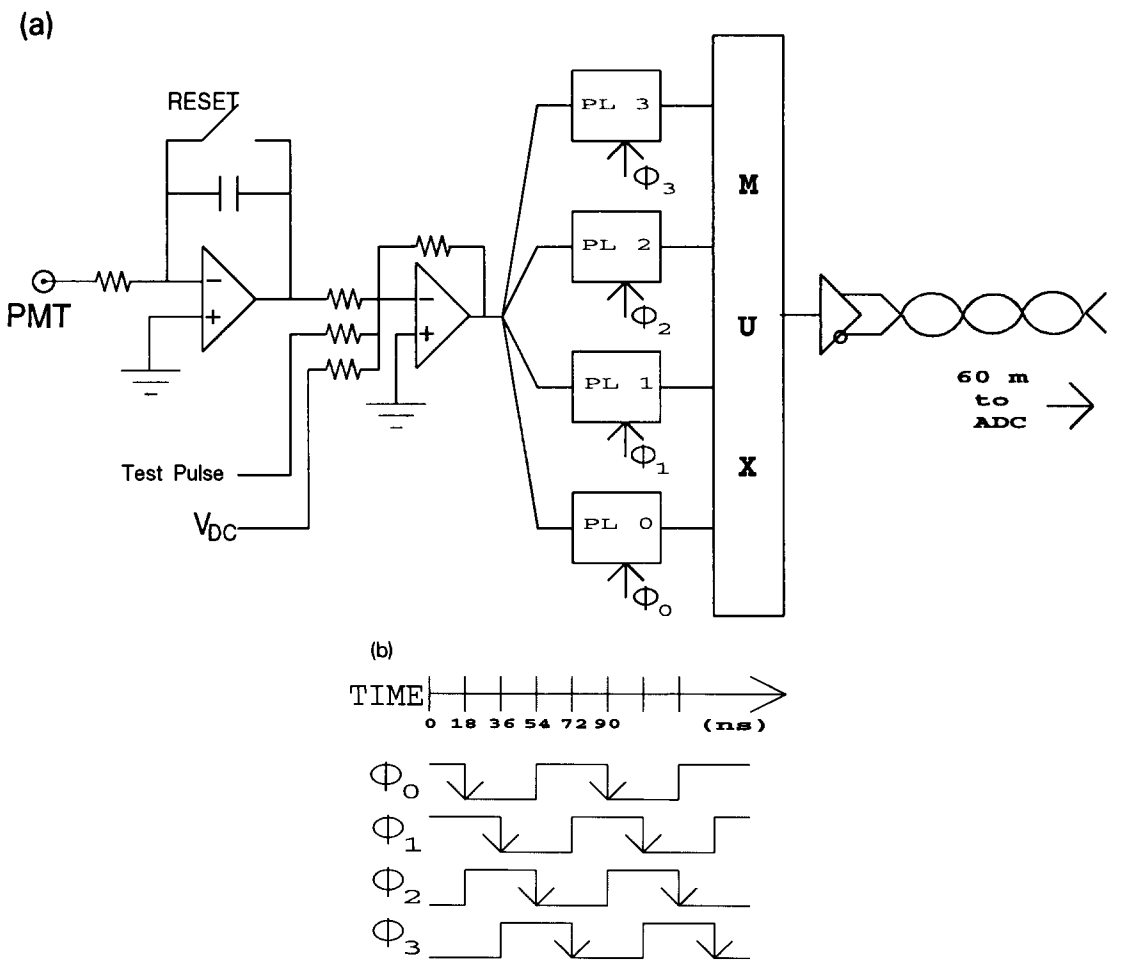

Fig. 3. (a) Schematic of one channel of the analog electronics. (b) Timing diagram for the clocks of the four analog pipelines, where the edges which result in the pipelines sampling the signal voltage are marked with arrows. The clock for PLn is denoted by ϕ_n.

Table 1
Summary of properties of the electronics.

Parameter	Value
Number of channels	192
Dynamic range	≈ 11 bits
Nonlinearity	< 0.5%
Sampling frequency	55.6 MHz
Variations in sampling time	< 1 ns
Integration time constant	≈ 6 ns
Max. number of samples digitized/trigger	224

inverted by a second op-amp, which also enables the introduction of a dc voltage or test pulse for calibration purposes. The output voltage of the op-amp is then sampled by four switched capacitor analog pipelines (PL0 through PL3) operating out of phase, as described below. Once a trigger has been received, the pipelines are stopped, and the samples read out through a multiplexer chip (MUX). Each MUX reads 16 different pipelines, corresponding to four PMTs. The output of each MUX is then digitized by a 1 MHz 12-bit ADC, located on a VME-based "Digital Card" of the ZEUS calorimeter readout [12].

Fig. 4 shows the circuit layout of the analog pipeline [13], designed for the ZEUS calorimeter readout and realized in 2.5 μm ± 5V CMOS technology. One chip contains four such pipelines, each 58 cells in length. Each of the 58 storage cells comprises a 1 pF capacitor, a common input bus for connecting one side of the capacitors to either the input or to ground, a CMOS switch for connecting the other side of the capacitors to ground while writing or to an output amplifier for reading, and a digital shift register for commutating the switches. Extensive tests performed on the pipelines [12,14] have shown that the dc and pulse nonlinearities are < 0.05% and < 0.2% respectively, over the input signal range of 0 → −2 V. The random noise with respect to the input is less than 0.3 mV rms. The cell-to-cell switching jitter is 0.1 ns, the input time

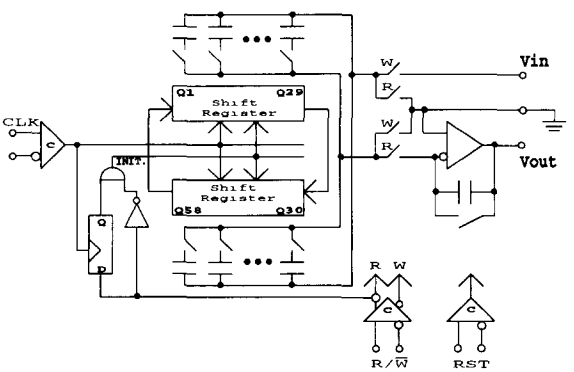

Fig. 4. Schematic of the ZEUS switched capacitor pipeline.

constant is 6 ns, and the maximum writing frequency is about 18 MHz.

Three NIM-based modules were constructed to provide the interface to the trigger system, control the number of samples per pipeline to be read out, generate the read and write clocks to the pipelines and MUX, handle the resetting of the integrators, and perform other control and calibration tasks. One control module digitally generates the four clocks (ϕ_0 through ϕ_3) which determine the times at which each pipeline samples the integrated signal voltage. By generating these clocks such that each comes 90° out of phase with the previous one, as depicted in fig. 3b, a four-fold increase in the sampling frequency is obtained. Thus, writing to each pipeline at 13.9 MHz yields an effective sampling frequency of 55.6 MHz. Reading 56 of the 58 samples in each of the four pipelines then yields 224 measurements of the integrated input signal, each separated by 18 ns, corresponding to a period of greater than 4 μs.

4.1. Calibration of the readout

The natural uranium radioactivity provides an important calibration source for the readout. Test beam measurements by the ZEUS collaboration [15, 16] have shown that cell-to-cell uniformities at the 1% level can be achieved by normalizing channel gains using the measured current through the PMTs (when no beam is present). The uranium activity is visible primarily as single photoelectrons with a rate of 2–10 MHz depending on the calorimeter section (EMC, HAC1, HAC2). The light collection efficiency is such that one photoelectron per PMT corresponds to approximately 10 MeV of deposited energy. The energy depositions due to individual uranium decays can be seen in fig. 5, an example of a sampled integrated PMT signal. For this figure, the PMT gain was increased by a factor of approximately 15 in order to make the depositions more clearly visible.

We used the integrated uranium current in order to normalize the individual channel gains. Due to the different thicknesses of the DU cladding, it is necessary to intercalibrate the EMC and HAC sections. The intercalibration was taken from the ZEUS BCAL testbeam results [16], where it was obtained by minimizing the hadronic energy resolution as a function of the intercalibration scale factor. This factor, which was determined to be independent of hadron energy, is known to better than 1%.

Several types of calibrations were applied to the data in the analysis stage. These included corrections for 1) individual pipeline cell gains and offsets; 2) overall channel gains; 3) integrated uranium activity; and 4) event-by-event baseline motion. The first three sets of corrections were derived from special runs with

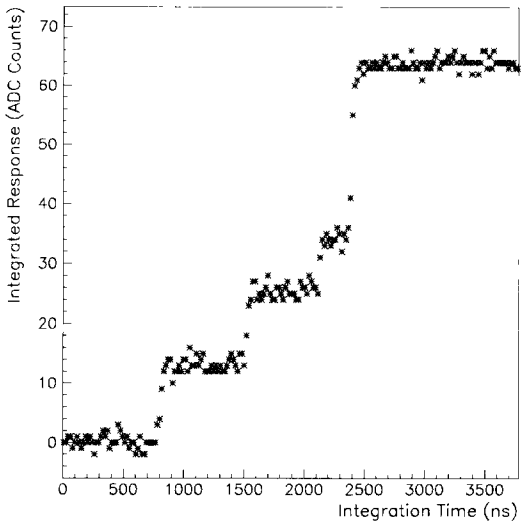

Fig. 5. Integrated PMT response to the signal produced by the natural radioactivity of the depleted uranium. Successive samples are separated by 18 ns. With the PMT gain set 15 times higher than the nominal setting, 1 ADC count corresponds to an energy deposit of approximately 0.7 MeV.

no input to the electronics beyond the uranium radioactivity, which was integrated with varying gate lengths. The linearity of the response was checked in this way to be within 0.5% over the full dynamic range. The fourth correction made use of samples arriving before the pulse and was calculated event-by-event.

For the beam measurements, the gain scale was set such that the readout electronics saturated for an energy deposition of approximately 40 GeV in a single cell. The noise level after all calibrations were applied had components due to electronic noise and to uranium activity. The noise was calculated as the rms of the corrected samples after baseline subtraction, for random triggers without beam. Typical noise levels as a function of integration time are summarized in table 2, where the integration time refers to the interval between the baseline samples and those used for the noise measurement. The noise can be parametrized as

$$\sigma^2 = \sigma_1^2 + \sigma_2^2 t(\mathrm{ns}),$$

with t being the integration time, $\sigma_1 = 20$ MeV, and $\sigma_2 = 0.9$, 2.0, 2.2 MeV for the EMC, HAC1 and HAC2 sections respectively. The σ_2 contributions for the various calorimeter sections are consistent with the uranium noise measured with the standard ZEUS readout electronics [17]. Their relative sizes are as expected from the dimensions of the cells and the thicker uranium plate cladding in the HAC sections. The value of σ_1 implies a dynamic range of the readout of approximately 11 bits.

Table 2
Noise per BCAL cell, in the different calorimeter sections, as a function of integration time.

Integration time (ns)	Noise/cell [MeV]		
	EMC	HAC1	HAC2
160	25	28	29
520	32	56	63
970	37	70	79
1510	43	84	90
3310	55	104	117

5. Beamline

The elements in the Fermilab NTE beamline at Lab E/F, which were installed and calibrated by the ZEUS collaboration for tests of the BCAL modules [16], are shown schematically in fig. 6.

The four BCAL modules were stacked on a computer-controlled fixture capable of independent rotation about the (ZEUS) θ and ϕ directions such that the beam particles entered the middle two calorimeter modules as if originating from the HERA mean interaction point. In these tests, the modules were positioned such that the showers were centered in the readout region. We also took data with the beam positioned near a corner of the instrumented region in order to study transverse leakage. To identify leakage energy from the rear of the BCAL modules, part of the CCFR neutrino experiment target [18] was used as a backing calorimeter (BAC).

The secondary beam, created from extracted 800 GeV protons hitting a Be target, comprised negatively charged pions, kaons, electrons, antiprotons, and muons. An array of scintillation counters provided the beam trigger, with a large veto counter rejecting beam halo events. A muon trigger was formed by requiring

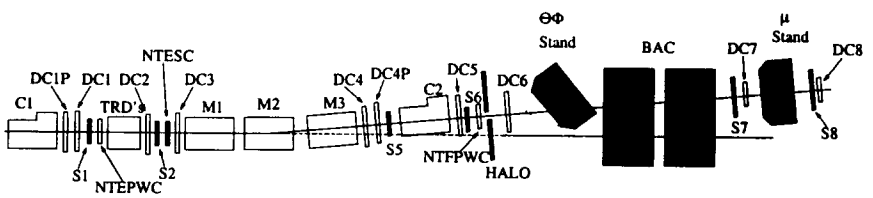

Fig. 6. Schematic of the E790 beamline elements at FNAL.

several elements downstream of the BAC in coincidence with the beam trigger. Electrons were selected using six TRD modules. Reference should be made to [16] for a more detailed description of the beamline.

The beamline elements were not read out for this study. Rather, the results from the ZEUS testbeam were used to set magnet currents and other parameters. As a result, event-by-event particle momentum corrections could not be made. The width of the momentum distributions was about 1% for pions and muons and, due to energy losses in the material of the beamline, several percent in the case of electrons.

The purity of the electron trigger was estimated from the ratio of energy deposited in the EMC section to the total energy. From these distributions, we find electron purities in excess of 99.5%. A similar procedure revealed that the electron contamination of the data sets for the 20, 50, and 100 GeV/c pion settings was at the level of 4%, 1%, and less than 0.1%, respectively.

The particle arrival time was asynchronous with the pipeline clock in order to provide continuous sampling on the rising edge of the calorimeter pulse. Channel-to-channel timing differences were kept to the order of 1 ns, and the particle arrival time was measured relative to the sampling clock with a TDC with 0.5 ns bin size.

6. Data analysis and results

The data sets taken during the short running period allocated to this study are listed in table 3, along with the number of events recorded. The labels in the table will be used in the following text to refer to the various data sets. The special calibration runs are not listed in the table.

Data quality cuts rejected between 10 and 15% of the events of the various data sets. The criteria included a minimum energy deposited in the BCAL modules by electron and pion candidates, and an event timing consistent with the RF structure of the beam. A further 26% of the 100 GeV/c pion data was rejected since one or more of the readout channels was saturated.

Table 3
The different sets of data recorded.

Label	Data Type	Mean momentum [GeV/c]	Number of events
L	laser	–	1000
M100	μ^-	100.0	10000
E16	e^-	15.6	20000
E41	e^-	40.8	20000
P20	π^-	19.6	40000
P50	π^-	49.8	20000
P100	π^-	100.0	40000

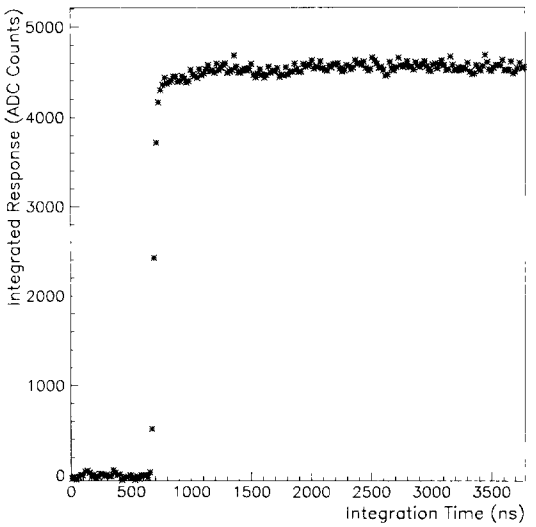

Fig. 7. Typical integrated response for a 41 GeV/c electron. Successive samples are separated by 18 ns. The vertical scale is in units of ADC counts, where 1 count corresponds to an energy deposit of 8.5 MeV.

A sample event from data set E41 is shown in fig. 7. The integrated pulseheight is shown versus time, with consecutive samples separated by 18 ns. The baseline has been adjusted using the presamples. Note that, since we read out many presamples, the pulse begins at a time of about 650 ns.

In analyses which examined the response averaged over many events, an event-by-event normalization was applied to remove fluctuations in the amount of energy deposited as well as beam momentum spread, as we were primarily concerned with the shape of the response versus time. The value near the end of the readout time was used to perform the normalization. In addition, the integration time was redefined to begin when the particle entered the calorimeter. Although the TDC time was used to measure the arrival time with a granularity of 0.5 ns, most results are presented in somewhat coarser time bins.

6.1. Response to laser pulses

The response to laser pulses was used to set a benchmark for the performance of the readout system. This test used the ZEUS laser calibration system [6], whereby 337 nm light pulses, shifted to 420 nm by a dye module, were sent via optic fiber to each PMT channel. The light was incident on a 10 cm long cylinder, composed of WLS material, placed directly in front of the PMT. This setup was chosen in order to

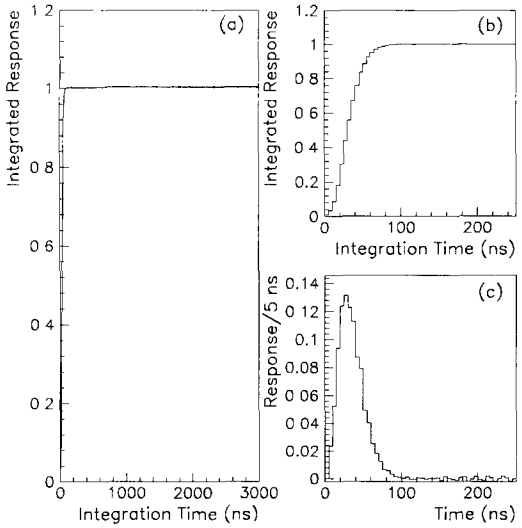

Fig. 8. Average integrated response to the laser signal vs time for (a) 3 μs, and (b) the first 250 ns. The integral is normalized to unity for an integration time of 100 ns. In (c) the signal time dependence, from "differentiating" the integrated response, is shown.

produce a spectral distribution at the PMT similar to that from particles. It was assumed that the time dependence of the light pulse arriving at the PMT would be very similar to that from prompt showers since the WLS time constants are present in both cases. As explained in the next section, this turned out not to be the case.

The integrated response for laser pulses is shown in fig. 8. All instrumented channels were summed to produce this plot (the typical channel received an amount of light comparable to that produced by a 2 GeV/c electron). The integral response is shown for a 3 μs period in fig. 8a, while the first 250 ns are shown expanded in fig. 8b. The integral of the pulse is flat after 100 ns, indicating that there are no long time constants introduced by the WLS. The laser light was transmitted to the WLS down a 60 m optic fiber; the $\approx 0.2\%$ increase in the integrated response after about 600 ns likely results from light reflections in the optical transmission.

It is possible to recover the input pulse shape by "differentiating" the integral with respect to time by taking successive differences. The result is shown in fig. 8c. The laser pulse shape is not perfectly smooth due to the small number of events in data set L. The rising edge is somewhat slower than that measured with a fast oscilloscope. This is primarily due to the integration time of the switched capacitor pipeline chips, which have an input time constant of 6 ns [14]. Variations in the sampling times of the different pipeline chips also produce a smearing of the order of 1 ns.

6.2. Response to electromagnetic showers

The average response versus time for data set E41 is shown in fig. 9. The response for set E16 was found to be very similar, indicating that the time development of electromagnetic showers is independent of the electron momentum in the measured range of approximately 15–40 GeV/c.

From fig. 9, it is clear that, unlike for the laser, the electron response is not fully saturated after 100 ns. Using the laser data to parametrize the prompt response, a fitting procedure was used to extract the electron shower time constants. Three extra exponential terms were needed to get a good fit to the data. The fitted time constants were (24.9 ± 0.5), (171 ± 20), and (1718 ± 100) ns. They contributed (6.4 ± 0.9), (3.2 ± 0.5), and $(3.6 \pm 0.2)\%$ of the total electron signal respectively, with $(86.8 \pm 1.0)\%$ of the energy being prompt. Thus, a substantial fraction of the electron response arrives after the first 100 ns, including a contribution of 3.6% which is collected with a time constant of 1.7 μs.

The long time constants in the electron response, and the lack of such an effect in the case of the laser (where the light goes only through the WLS), suggest a long decay time component in the scintillator response. Indeed, 100 GeV/c muons passing through the BCAL modules were seen to produce the same time response

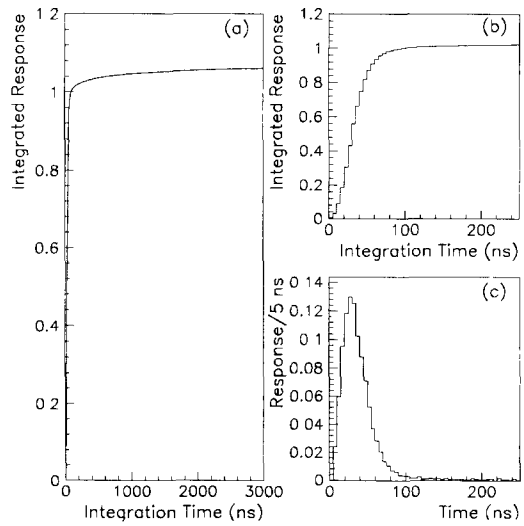

Fig. 9. Average integrated response to 41 GeV/c electrons vs time for (a) 3 μs, and (b) the first 250 ns. The integral is normalized to unity for an integration time of 100 ns. In (c) the signal time dependence, from "differentiating" the integrated response, is shown.

as electrons. Long time constants in the scintillator were searched for in separate measurements at Nevis Labs where, after reproducing the laser measurements from FNAL with laser light directed into the WLS, a single scintillator layer of a test stand which mimics an EMC cell was exposed to UV light (337 nm). No long time constants were seen. However, measurements using cosmic muons did show the late energy component. The possibility that the effect is introduced due to the presence of the depleted uranium was ruled out by the fact that, even with the DU plates removed from the stack, the late energy component was still present. In conclusion, the long time constants are introduced by the scintillator response, and arise only from energy depositions from particles.

6.3. Response to hadronic showers

The integrated response of the BCAL to pions of different energies is shown in fig. 10, superimposed on the laser and electron responses. The results are summarized in table 4. Comparing the pion response to that of electrons, it is apparent that a substantial fraction of the pion signal is deposited late in the shower development. While the long time component seen for the electron response explains some of the delayed energy in the pion signal, there is a large excess of late energy above this contribution, which must come from energy depositions peculiar to hadron showers. As discussed previously, such depositions are expected due to relatively slow nuclear processes initiated by the hadron shower, such as the emission of photons from nuclei which have become excited after absorbing a thermalized neutron.

A comparison of the data for 20, 50 and 100 GeV/c pions shows that the higher energy showers exhibit a lower fractional increase at later times. This result is consistent with the expectation that the contribution of the electromagnetic component of the hadronic shower, which results from π^0 production, should rise logarithmically with energy.

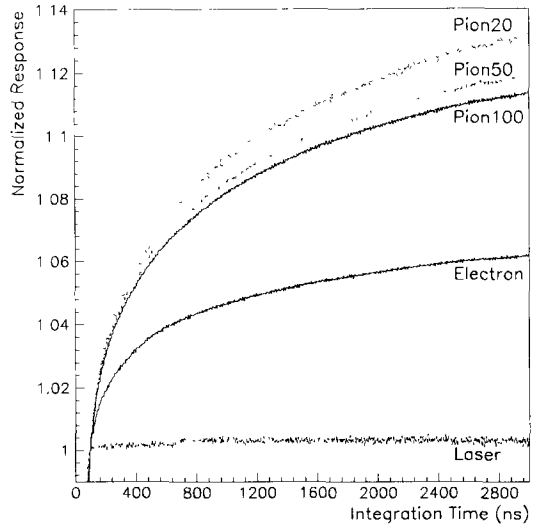

Fig. 10. Average integrated response for data sets L, E41, P20, P50, P100 vs time. The integrals are normalized to unity for an integration time of 100 ns. Note the suppressed zero on the vertical axis.

The measured time profile for a hadronic shower is the convolution of the time profile of the hadronic energy deposition with the response of the optical components and readout electronics. These must be deconvoluted in order to compare our measurements with the predictions from MC calculations. We have assumed that the signal for electromagnetic showers measures the response of the entire system, including optical components and read-out electronics, to prompt energy deposits in the scintillator. This assumption is supported by the very similar integrated responses measured for muons and for electrons.

Table 4
Integrated signals versus integration time for the various data sets. The integrated signals are normalized to unity for an integration time of 100 ns. The errors are dominated on the rising edge by timing uncertainties, and by systematic uncertainties in the uranium current subtraction for longer integration times. The errors for the laser are larger than for the beam data due to statistics.

Time [ns]	Normalized value of integrated signal				
	Laser	E41	P20	P50	P100
20	0.180 ± 0.010	0.185 ± 0.010	0.145 ± 0.010	0.160 ± 0.010	0.161 ± 0.010
50	0.837 ± 0.005	0.819 ± 0.005	0.762 ± 0.005	0.777 ± 0.005	0.777 ± 0.005
100	1	1	1	1	1
200	1.002 ± 0.001	1.0190 ± 0.0001	1.0316 ± 0.0002	1.0307 ± 0.0001	1.0299 ± 0.0001
500	1.001 ± 0.001	1.0359 ± 0.0001	1.0661 ± 0.0003	1.0619 ± 0.0001	1.0593 ± 0.0001
1000	1.003 ± 0.001	1.0465 ± 0.0001	1.0938 ± 0.0005	1.0849 ± 0.0002	1.0816 ± 0.0001
2000	1.003 ± 0.001	1.0563 ± 0.0002	1.1168 ± 0.0010	1.1073 ± 0.0004	1.1030 ± 0.0002
3000	1.003 ± 0.001	1.0620 ± 0.0002	1.1321 ± 0.0015	1.1187 ± 0.0006	1.1139 ± 0.0003

Table 5
Result of the fits of the pion response. The parameters are defined in eq. (2). The values for the amplitudes are quoted as percentages of their sum.

Pion set	Fitted value of parameter						
	A_0 [%]	A_1 [%]	τ_1 [ns]	A_2 [%]	τ_2 [ns]	A_3 [%]	τ_3 [ns]
P20	49.6 ± 3.0	42.9 ± 3.0	–	1.9 ± 0.3	136 ± 30	5.6 ± 0.2	1316 ± 200
P50	59.3 ± 3.0	34.4 ± 3.0	–	1.7 ± 0.3	102 ± 25	4.6 ± 0.2	1129 ± 150
P100	58.4 ± 3.0	36.0 ± 3.0	8.8 ± 1.0	1.6 ± 0.3	128 ± 20	4.0 ± 0.2	1166 ± 100

Different methods were attempted to extract the hadronic shower time profile, including numerically deconvoluting analytic functions which had been fitted to the pion and electron signals. The most stable method resulted from using the measured electron signal from fig. 9 to parametrize the prompt response, and folding it with test functions to represent the hadronic shower time profile. The measured normalized time response of the pion showers, $p(t)$, was thus modelled as a convolution of the electron response with a function, $h(t)$, describing the time spectrum of the deposited energy:

$$p(t) = \int_0^t e(t-t')h(t')\,\mathrm{d}t', \tag{1}$$

where

$$h(t) = A_0\,\delta(t) + \sum_{i=1}^{3} \frac{A_i}{\tau_i}\exp(-t/\tau_i). \tag{2}$$

The first term in $h(t)$, where $\delta(t)$ is the Dirac delta function, was included to describe the fraction of the pion energy deposition which is similar to an electromagnetic shower or minimum ionizing particle and, therefore, prompt. A minimum of three exponential terms in $h(t)$ was necessary to achieve a good description of the data and to get flat residual distributions. Including additional terms did not significantly improve the quality of the fits.

Due to the sensitivity of the fitting on the fast rising edge of the pulse, a large correlation was found between parameters A_0, A_1, and τ_1. Parameter τ_1 was fit for set P100 where the data errors are smallest, yielding a fitted value of (8.8 ± 1.0) ns. For the other two data sets, τ_1 was fixed at 9 ns. The results of the fits are given in table 5.

Within the energy regime under study here, the physical processes contributing to hadronic showers are expected to be the same at all energies, and should therefore produce characteristic time constants. As can be seen from table 5, the fitted values of the longer time constants, τ_2 and τ_3, are indeed consistent for the three data sets. The results were combined to yield the final values $\tau_1 = (9 \pm 1)$ ns, $\tau_2 = (120 \pm 20)$ ns and $\tau_3 = (1160 \pm 100)$ ns, after taking into consideration the estimated fitting errors for the different data sets.

To extract the contributions of the different components of the signal, the data were fitted with the time constants fixed to their central values. The results are given in table 6. The errors were estimated from the stability of the fit parameters and by comparing the results from fits using different distributions (e.g. using electron set E16 rather than E41).

Table 6
Result of the fits of the pion response with fixed time constants $\tau_1 = 9$ ns, $\tau_2 = 120$ ns, $\tau_3 = 1160$ ns. The parameters are defined in eq. (2).

Pion set	Fitted value of parameter			
	A_0 [%]	A_1 [%]	A_2 [%]	A_3 [%]
P20	50.0 ± 2.0	42.8 ± 2.0	1.4 ± 0.2	5.8 ± 0.1
P50	57.5 ± 2.0	36.4 ± 2.0	1.6 ± 0.2	4.5 ± 0.1
P100	59.6 ± 2.0	34.7 ± 2.0	1.6 ± 0.2	4.1 ± 0.1

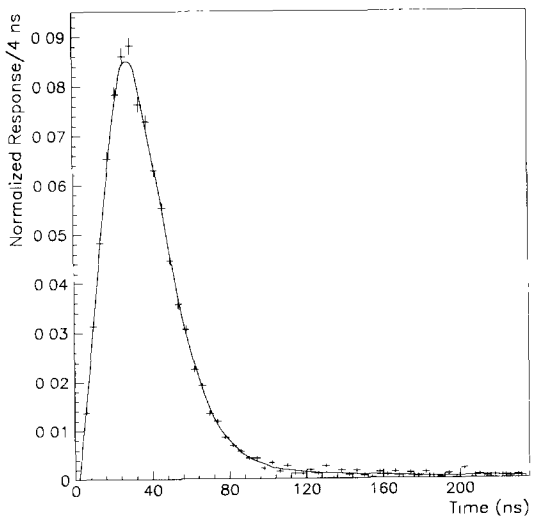

Fig. 11. The result of the fit described in the text of the 50 GeV/c pion data. The "differentiated" signal is presented to show the quality of the fit on the rising edge of the integrated pulse. The data points are the 50 GeV/c pion data, while the curve is the result of the fit.

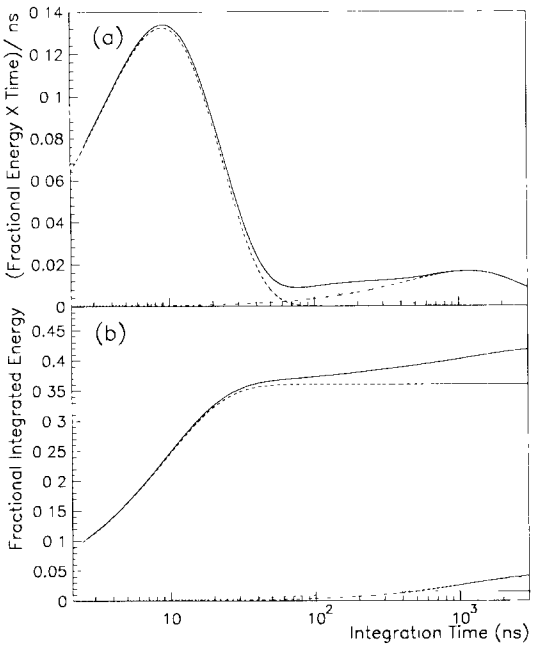

Fig. 12. (a) Lethargy plot from the fitted time spectrum for 50 GeV/c pions, and (b) the integrated fractional energy vs time. The solid line shows the sum of the three exponential terms described in the text, while the others represent their individual contributions. The prompt component is not shown in the figure.

The quality of the fit can be judged from fig. 11. In this figure, the derivative of the measured hadron response is shown along with the fit. The data are well described by the fitted curve, and the fit improves further for longer times where the slope of the integrated signal is small.

The contribution of the delayed signal is the sum of terms A_1, A_2, and A_3, and contributes 40 to 50% of the total. This value is in good agreement with ref. [4] which predicts that 40% of the signal is delayed for 10 GeV pions. The contribution from the prompt component, given by A_0, indeed shows the expected trend of increasing with pion energy. The fractional contribution of the long time constant, A_3, has the smallest error, and its decrease with energy shows the trend in a clear way.

Given the fit parameters, it is possible to plot the time spectrum of the hadronic energy deposition. The results for data set P50 are shown in a lethargy plot in fig. 12a, while the integrated late component is shown in fig. 12b. These results are to be compared to the MC predictions from ref. [4] which were shown in figs. 1a and 1b. The short time constant has the expected value of about 9 ns, but the other two time constants are longer than expected. In fact, the longest time constant is considerably larger, and contributes less to the total signal, than predicted. The parameters A_3 and τ_3 are well measured and relatively uncorrelated with other parameters, so the disagreement is not due to fitting uncertainties. Thus, while the total contribution from late energy deposits agrees with the prediction, the increase of the measured signal after 100 ns is weaker than expected and proceeds with longer time constants.

6.4. Development of the hadronic shower profile

The longitudinal and transverse segmentation of the BCAL enables the study of the time development of the shower profile for hadronic showers. The shower depth can be studied using the signals in the three longitudinal sections of the BCAL. The transverse granularity is much finer; a total of 64 EMC cells (each of dimensions of about 5 cm × 20 cm, with an effective Molière radius on order of 2 cm) were instrumented, along with 24 cells (approximately 23 cm × 30 cm) of each of the HAC1 and HAC2 sections.

For 50 GeV/c pions, the fractional contributions of the individual sections to the total signal were 22%, 54%, and 24% for EMC, HAC1, and HAC2 respectively. Fig. 13a shows the response vs time for the three sections separately, where the three curves have been normalized to unity for an integration time of 100 ns.

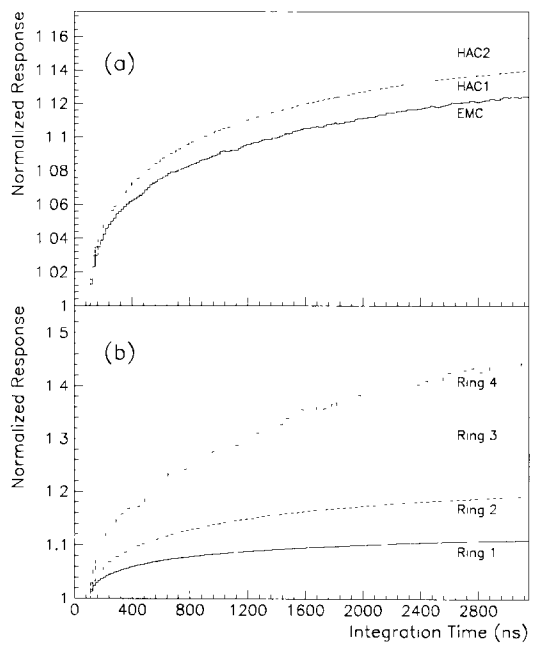

Fig. 13. (a) Normalized response vs integration time, for 50 GeV/c pions, for the contributions to the total signal seen (a) in the EMC, HAC1, and HAC2 sections, and (b) in the lateral "rings" defined in the text. For both plots, the integrals are normalized to unity for an integration time of 100 ns, and successive time bins are separated by 18 ns.

Clearly, the energies deposited at greater depths in the shower reveal larger fractional contributions from the late components. While the EMC energy increases by about 12% between 100 ns and 3 μs, the corresponding increases for HAC1 and HAC2 are 14% and 16%, respectively.

To investigate the lateral spread of 50 GeV/c pion showers, the instrumented cells were divided into four lateral "rings", according to their mean fractional contribution to the total signal. The first ring, or shower core, contained those cells which contained, on average, at least 10% of the total deposited energy; it comprised one EMC cell, two HAC1 cells, and one HAC2 cell. The second ring contained all cells (two EMC, two HAC1, and three HAC2) which contained, on average, less than 10% but more than 1% of the total energy. The third ring contained the 8 EMC, 7 HAC1, and 7 HAC2 cells whose average contributions were less than 1% but greater than 0.1%. Finally, the fourth ring comprised the remaining 53 EMC, 13 HAC1, and 13 HAC2 cells, each of which contributed less than 0.1% to the total signal. The contributions of the individual rings to the total energy were, proceeding from ring 1 through ring 4, 79%, 13%, 5%, and 3% respectively.

Fig. 13b shows the normalized contributions to the integrated response vs time as measured in the four lateral rings separately. Clearly, those rings which are farther from the shower core display larger fractional contributions from the late components of the shower. The fractional increases between 100 ns and 3 μs were about 11%, 19%, 34%, and 44% for rings 1 through 4, respectively.

In conclusion, the late components of hadronic showers diffuse more uniformly through the calorimeter than does the more well collimated shower core. Thus, calorimeter cells which are situated at a larger distance from the shower centroid receive a larger fraction of their energy from the late depositions.

6.5. Compensation and energy resolution vs integration time

The differences in the time distributions of the electron and pion responses imply that the ratio of the electron signal to the hadron signal, and therefore the degree of compensation, is a function of the time over which the signal is integrated. This effect is expected, in turn, to cause an integration time dependence of the hadronic energy resolution.

To make a direct comparison of the electron response with the pion response, we fitted a Gaussian to the peak of the deposited energy distributions for pions and electrons, and used the conversion from magnet current setting to particle momentum to derive a scale factor for the normalized integral plots. This normalization procedure removes to a large extent the effect of energy leakage in the pion events.

The uncertainty in the normalization procedure was estimated from the consistency of the measured signals for the different particle types and momenta. The three pion data sets yielded, to within ±0.5%, the same conversion from ADC counts of measured signal to GeV/c of incident momentum. The agreement between the two electron data sets was at the ±0.8% level. From this data, we estimate the systematic error in the scale factor derived for comparing the pion and electron signals to be 1%.

With this scale factor, the ratio of electron to pion response (e/π) was measured to have a value of 1.02 ± 0.01 for an integration time of 100 ns and for particles of 20 GeV/c momentum. The results for all three

Table 7
Values of e/π as a function of integration time for the various pion data sets, using set E41 for the electrons. The errors quoted are those due to the timing precision of ±0.25 ns as well as systematic uncertainties in the uranium current subtraction. There is an additional systematic uncertainty of ±0.01 in the overall scale at each energy.

Integration time [ns]	Ratio of electron to pion signal		
	P20	P50	P100
20	1.30 ±0.11	1.18 ±0.08	1.16 ±0.08
40	1.145 ±0.015	1.101 ±0.013	1.088 ±0.013
60	1.066 ±0.010	1.049 ±0.008	1.037 ±0.008
80	1.032 ±0.008	1.025 ±0.006	1.014 ±0.006
100	1.0184 ± 0.0040	1.0157 ± 0.0025	1.0048 ± 0.0025
200	1.0060 ± 0.0002	1.0042 ± 0.0001	0.9942 ± 0.0001
500	0.9896 ± 0.0004	0.9909 ± 0.0001	0.9826 ± 0.0001
1000	0.9744 ± 0.0005	0.9798 ± 0.0002	0.9722 ± 0.0002
2000	0.9632 ± 0.0009	0.9689 ± 0.0005	0.9623 ± 0.0003
3000	0.9554 ± 0.0013	0.9643 ± 0.0006	0.9580 ± 0.0003

pion data sets are summarized in table 7. The measured values of e/π are shown vs integration time in fig. 14a for 20 GeV/c pions.

The dependence of the energy resolution on integration time was examined for the 20 GeV/c pion data. After removing leakage by placing a 300 MeV cut on the BAC energy, Gaussian fits to the pulse height spectra were performed for different integration times. The results are shown in fig. 14b. The solid data points represent the raw resolution taken directly from the fits. In order to isolate the contributions to the resolution from fluctuations in the hadronic showers, the data were corrected for electronic and uranium induced noise. The corrected data are shown by the open circles in fig. 14b. As can be seen, the resolution degrades rapidly for integration times below 60 ns. This is due primarily to the smaller fraction of the pulse which arrives within the gate. For integration times ranging from 100 ns to 1 μs, the resolution remains relatively constant at the level of $35\%/\sqrt{E}$, a value consistent with that achieved by the ZEUS collaboration with readout electronics having a effective gate width of 130 ns [15,16]. For longer integration times, the resolution degrades even after removing the uranium noise. This behavior is expected from the deviation of e/π from unity.

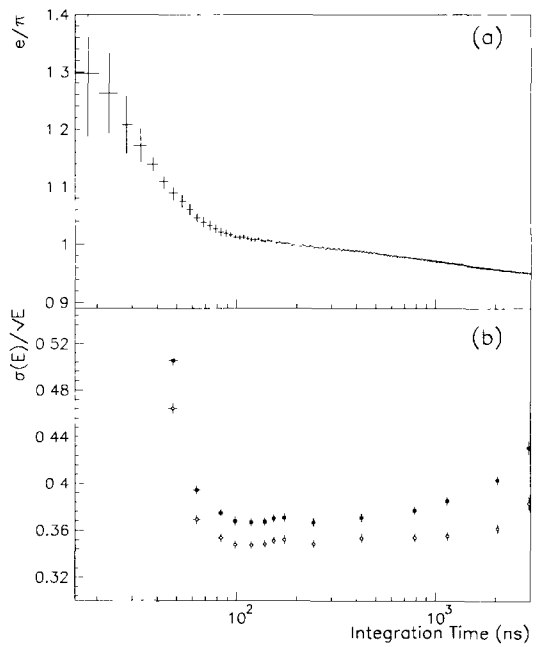

Fig. 14. (a) The ratio of electron to pion response vs integration time for 20 GeV/c pions. In addition to the errors shown, there is a systematic uncertainty of ± 0.01 in the overall scale. (b) The energy resolution, $\sigma(E)/\sqrt{E}$, vs integration time for 20 GeV/c pions. The solid points are for uncorrected data, while the open circles have electronic and uranium noise subtracted.

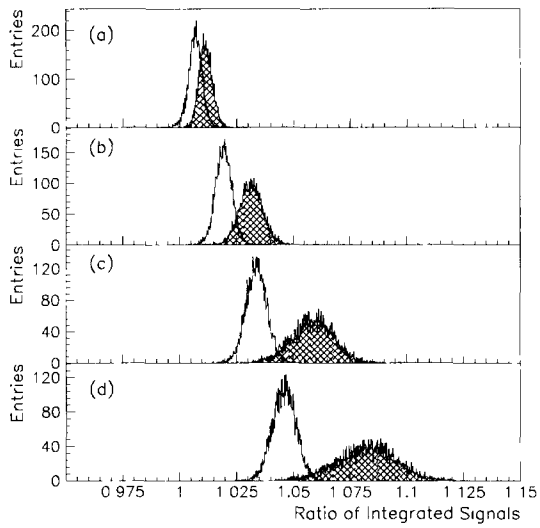

Fig. 15. Ratios of signals for different integration times for 50 GeV/c electrons (empty) and 100 GeV/c pions (hashed). The ratios used are (a) 200 ns/100 ns, (b) 400 ns/100 ns, (c) 1 μs/100 ns, (d) 3 μs/100 ns.

6.6. Electron–pion separation

The differences in the time distributions of the electron and pion responses allow for some particle discrimination based on timing information [19]. Only cells with a signal at least three times the noise were used in this analysis. Electron candidates were selected by requiring that the fractional energy deposited in the EMC be at least 95%, while pions have less than 95% of the energy deposited in the EMC. Events with large amounts of energy leakage were rejected by placing a cut on the minimum visible energy in the BCAL modules of 70 GeV for set P100 and 30 GeV for sets E41 and P50.

Fig. 15a shows, for sets E41 and P100, the distribution of events according to the ratio of the signal after an integration time of 200 ns relative to that after 100 ns. The distributions obtained for the ratio of the signal after 400 ns, 1 μs, and 3 μs relative to 100 ns are shown in figs. 15b, 15c, and 15d, respectively. Clearly, placing a cut on such ratios can be used to discriminate between electrons and pions. The purity and efficiency which can be attained are shown in fig. 16, where the efficiency for electrons passing a cut on the ratio is displayed vs the efficiency for pions to pass the same cut. A rejection factor of greater than 100 can be achieved for pions, while maintaining good electron efficiency. The results for 3 μs are summarized in table 8. The separation power degrades for lower pion energies despite the fact that these pions have a larger late energy component. For example, with an electron efficiency of 77.5%, the rejection factors for 100, 50, and

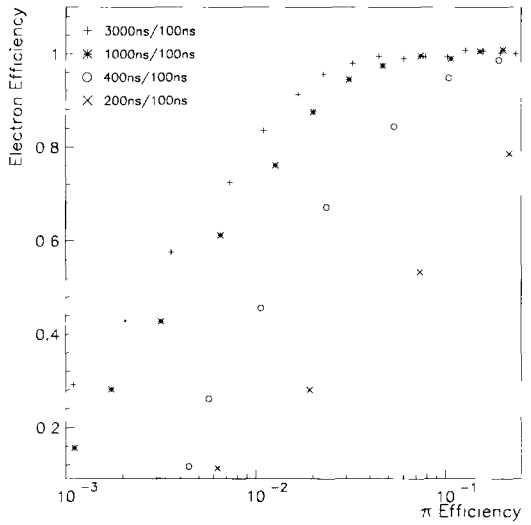

Fig. 16. The efficiency for 50 GeV/c electrons to pass a cut on the energy ratio vs the efficiency for 100 GeV/c pions to pass the same cut, for different integration times relative to 100 ns.

20 GeV/c pions are approximately 110, 25, and 5, respectively. This is due to the fractionally larger noise contribution at low energy, and to the rather low light yield of the ZEUS calorimeter. Calorimeters with higher light yields would have smaller fluctuations of the late signal, and should therefore gain in rejection power.

As can be seen in fig. 16, the separation between electrons and pions improves for longer integration times. The rejection power using ratios at different times, and for fixed electron efficiencies, are given for pions from set P100 in table 9. For example, with an electron efficiency of 60%, pion rejection factors of 250, 160, 52, and 10 are achieved using integration times of 3 μs, 1 μs, 400 ns, or 200 ns, respectively. Thus, although the noise increases for longer integration times, this is more than compensated by the increasing separation between the electron and pion signal levels.

6.7. *Implications for fast readout schemes*

In the high rate environments of present and future hadron colliders, the large flux of particles striking the calorimeter leads to a level of pile-up which contributes to the noise in the energy measurements. To reduce the sensitivity to pile-up, it is usual to employ a fast readout scheme, where only the first 100 ns or less of the deposited energy is used in the reconstruction of the incident particle's energy and arrival time.

The late components observed in hadronic showers will contribute to the levels of pile-up noise. However, the time constants involved are long compared to typi-

Table 8
Fraction of electrons and pions passing a cut on the ratio of the integrated energy after 3 μs compared to that after 100 ns.

Value of cut	Fraction of particles passing cut			
	41 GeV/c electrons	20 GeV/c pions	50 GeV/c pions	100 GeV/c pions
1.058	0.987 ± 0.001	0.459 ± 0.004	0.106 ± 0.004	0.038 ± 0.0024
1.056	0.969 ± 0.002	0.386 ± 0.004	0.087 ± 0.004	0.026 ± 0.0020
1.054	0.937 ± 0.003	0.321 ± 0.004	0.067 ± 0.003	0.019 ± 0.0017
1.052	0.870 ± 0.004	0.256 ± 0.004	0.052 ± 0.003	0.013 ± 0.0015
1.050	0.775 ± 0.005	0.197 ± 0.003	0.040 ± 0.003	0.0090 ± 0.0012
1.048	0.642 ± 0.006	0.148 ± 0.003	0.027 ± 0.002	0.0051 ± 0.0009
1.046	0.493 ± 0.006	0.108 ± 0.003	0.019 ± 0.002	0.0026 ± 0.0006
1.044	0.346 ± 0.006	0.076 ± 0.002	0.014 ± 0.002	0.0019 ± 0.0006
1.042	0.216 ± 0.005	0.050 ± 0.002	0.0092 ± 0.0013	0.00032 ± 0.00023
1.040	0.123 ± 0.004	0.032 ± 0.002	0.0064 ± 0.0011	0.00032 ± 0.00023

Table 9
For fixed electron identification efficiencies, the fraction of 100 GeV/c pions passing the cut on the ratio of integrated energies.

Integration times used in energy ratio	Fraction of 100 GeV/c pions passing cut on energy ratio	
	Electron efficiency = 60%	Electron efficiency = 80%
200 ns/100 ns	0.096 ± 0.004	0.226 ± 0.004
400 ns/100 ns	0.019 ± 0.002	0.039 ± 0.003
1.0 μs/100 ns	0.0062 ± 0.0009	0.016 ± 0.0016
3.0 μs/100 ns	0.0040 ± 0.0008	0.010 ± 0.0013

cal bunch crossing times, so the effect will be to produce shifts in the baseline. These shifts can be easily subtracted with an appropriate readout scheme. However, there are also effects at short times, as can be seen in fig. 14. The value of e/π and the resolution depend very strongly on the integration time for times less than 60 ns. The differences in pulse shape for electrons and hadrons can also result in shifts in the time which would be reconstructed.

As an example of the magnitude of these effects, we consider the ZEUS readout scheme [12], where the PMT pulse is shaped by a four stage shaping circuit with an impulse response function

$$Z(t) = \frac{t^3}{6\tau^4}\exp(-t/\tau), \qquad (3)$$

with $\tau = 33$ ns. The shaped pulse is sampled every 96 ns by switched capacitor pipelines. This circuit, in conjunction with the energy reconstruction algorithm, yields an effective integration gate width of 130 ns. The data in fig. 14 would then predict a value of e/π of 1.02 ± 0.01 and a hadronic energy resolution of $35\%/\sqrt{E}$. Due to the differences in the time evolution of the signals from electrons and hadrons, the time of the peak of the shaped pulse depends on particle type. Convoluting the measured pulse shapes (see fig. 10) with the form of $Z(t)$ above shows that the peak for electrons is shifted by 1 ns relative to a laser pulse, while that for 20 GeV pions is shifted an additional 3 ns. For a hadronic shower, the time of the peak of the pulse also depends on the location within the shower. Convoluting the measured time spectra of fig. 13a with the ZEUS shaping function reveals that, compared to the signal in the EMC, the peaks in HAC1 and HAC2 cells are shifted by an average of 0.8 ns and 1.2 ns respectively. The effect is more dramatic in terms of transverse distance from the shower center. For the lateral rings defined in section 6.4, the peak times in rings 2, 3, and 4 are shifted by 2.9 ns, 9.4 ns, and 9.7 ns relative to the central ring. The resulting shaped pulses for rings 1 and 4 are shown in fig. 17.

For the ZEUS readout scheme, the effect of the late energies on the energy resolution is negligible given the rather long effective integration gate. However, distinct time shifts are indeed observed. Schemes with much shorter integration times would show smaller time shifts, but would have degraded energy resolutions.

The long time components observed both in the response to hadrons and electrons depend on several factors. The time constants in the optical readout affect all particle types, while the late energy deposits arising from the choice of ^{238}U as absorber material predominantly affect hadronic showers. The late energy deposits also depend strongly on the sampling

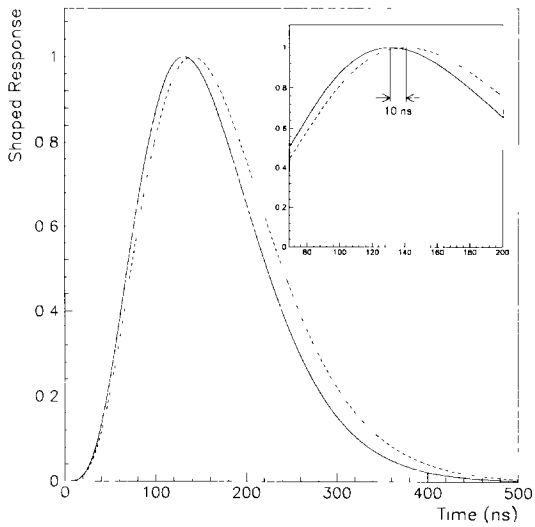

Fig. 17 The resulting pulse shape with the ZEUS readout electronics for cells in ring 1 (solid curve) and for cells in ring 4 (dashed curve). The late energy deposits produce a 10 ns shift in the position of the peak of the pulse. For a definition of the rings, see section 6.4.

layers, with hydrogenous materials being more sensitive to neutron energies. The readout electronics can also introduce time constants; in our case, an effective integration time constant of 6 ns was present from the electronics. The importance of the late time components for energy and time reconstruction therefore depend strongly on the calorimeter properties and readout scheme chosen.

7. Conclusions

We have measured the time evolution of particle showers in ZEUS barrel calorimeter modules. As expected, the response to hadronic showers includes substantial contributions from energy depositions which occur late in the shower development. The prediction that showers of hadrons of higher energy would more closely resemble electromagnetic showers was also verified.

An unexpected feature of the measured pulse shapes was the long time component present in electron showers. Tests showed that this component *is not* present when light pulses are used to excite the wavelength shifter or scintillator, but *is* present when muons traverse the scintillator. We conclude that charged particles produce long lived states in the scintillator, resulting in a significant fraction of the signal (on the order of 7%) arriving after 100 ns. Several time constants are involved; the longest measured component contains

approximately 3.6% of the signal and has a time constant of about 1.7 μs.

The different components of the time spectrum for hadron energy depositions were extracted using a fitting procedure. A value of about 40% was measured for the total fractional contribution from the late energy deposits, including over 5% which is deposited with time constants greater than 100 ns. While the overall level is consistent with expectations, a more detailed examination of the results reveals only qualitative agreement with Monte Carlo predictions. The time profile for hadron showers was measured as a function of longitudinal and lateral depth. Cells which are farther away from the shower maximum contain a higher fraction of late energy, illustrating that the sources of the late depositions diffuse with a higher effective mean free path through the calorimeter.

The ratio of the response to electrons to that of hadrons was determined to be 1.02 ± 0.01 for an integration time of 100 ns, in agreement with previous measurements. The resolution for hadronic showers was found to depend strongly on the integration time for integration times of less than 60 ns. The resolution was flat within our measurement error at a level of $35\%/\sqrt{E}$ for integration times between 100 ns and 1 μs.

The difference in the time spectrum for electromagnetic and hadronic showers can be exploited to identify the particle type. Cutting on the ratio of the signal at late times to that at early times can give pion rejection factors in excess of 100 with electron efficiencies greater than 60%. This technique was limited in these measurements by the rather large contribution from electronic noise, and the relatively small light collection efficiency of the ZEUS calorimeter modules.

Acknowledgements

We would like to acknowledge the efforts of the administration and staff of Fermilab, without which the testbeam program for the ZEUS BCAL modules would not have been possible. We thank the members of the ZEUS BCAL testbeam collaboration (E790) for generously providing the beamtime for these measurements. In particular, we would like to thank Steven Ritz for providing us with the run control system.

We greatly appreciate many useful discussions with Robert Klanner.

The excellent work of Herb Cunitz and the Nevis Labs electronics shop are gratefully acknowledged.

We would like to thank U. Behrens for permission to reprint figs. 1a and 1b, which were taken from ref. [4].

This research has been supported in part by National Science Foundation grant PHY-89-21320, by Department of Energy grant DE-FG02-90ER40540, and by Columbia University. One of us (J.P.) would like to acknowledge financial support from the Natural Sciences and Engineering Research Council of Canada.

References

[1] C. Fabjan et al., Nucl. Instr. and Meth. 141 (1977) 61.
[2] For example, see R. Klanner, Nucl Instr. and Meth. A265 (1988) 200.
[3] J Brau and T. Gabriel, Nucl. Instr. and Meth. A238 (1985) 489.
[4] H. Brückmann et al., Nucl. Instr. and Meth. A263 (1988) 136.
[5] R. Wigmans, Nucl. Instr. and Meth A259 (1987) 389
[6] ZEUS Detector Technical Proposal (1986);
The ZEUS Detector, Status Report (1989), DESY PRC 89-01.
[7] M. DeVincenzi et al., Nucl. Instr. and Meth. A243 (1986) 348;
M.G. Catanesi et al., Nucl. Instr. and Meth. A260 (1987) 43;
T Akesson et al., Nucl. Instr. and Meth. A262 (1987) 243.
[8] J.A. Parsons et al., Proc. 2 nd Int. Conf. on Calorimetry in High Energy Phys., Capri (1991) 184.
[9] M. Derrick et al., Nucl. Instr. and Meth A309 (1991) 77.
[10] B. Bylsma et al., Nucl. Instr. and Meth. A305 (1991) 354.
[11] A. Caldwell et al., Proc. 1st Int. Conf. on Calorimetry in High Energy Phys., FNAL (1990) 243.
[12] A. Caldwell et al., Nucl. Instr and Meth. A321 (1992) 356.
[13] J. Möschen et al., Nucl. Instr. and Meth. A288 (1990) 180.
[14] L. Hervás, Ph.D. Thesis, Universidad Autónoma de Madrid (1990). Also available as DESY Report F35D-91-01 (1991).
[15] A. Andresen et al., Nucl. Instr. and Meth. A309 (1991) 101.
[16] U. Mallik et al., Proc. 1st Int. Conf. on Calorimetry in High Energy Phys., FNAL (1990) 116;
I. Gialas et al., Proc. 2 nd Int. Conf. on Calorimetry in High Energy Phys., Capri (1991) 162.
[17] A. Bernstein et al., ZEUS Internal Note 91-114 (1991).
[18] W.K. Sakumoto, Nucl. Instr. and Meth. A294 (1990) 179.
[19] A. Caldwell and F. Sciulli, ZEUS Internal Note 88-84 (1988);
A. Caldwell, ZEUS Internal Note 89-75 (1989);
R. DeSalvo et al., Nucl. Instr and Meth. A279 (1989) 467;
D. Acosta et al., Nucl. Instr and Meth A302 (1991) 36.